

Article

Cu Nanoparticles Modified Step-Scheme Cu₂O/WO₃ Heterojunction Nanoflakes for Visible-Light-Driven Conversion of CO₂ to CH₄

Weina Shi ¹, Ji-Chao Wang ^{2,3,*} , Aimin Chen ¹, Xin Xu ¹, Shuai Wang ¹, Renlong Li ², Wanqing Zhang ² and Yuxia Hou ^{2,*}

¹ School of Chemistry and Materials Engineering, Xinxiang University, Xinxiang 453000, China; shiweina516@163.com (W.S.); chenaimin1978@163.com (A.C.); xuxin202111@163.com (X.X.); wangshuai00129@163.com (S.W.)

² College of Chemistry and Chemical Engineering, Henan Institute of Science and Technology, Xinxiang 453000, China; rlli@hist.edu.cn (R.L.); zhangwqzzu@163.com (W.Z.)

³ College of Chemistry, Zhengzhou University, Zhengzhou 450000, China

* Correspondence: wangjichao@hist.edu.cn (J.-C.W.); yxhou@163.com (Y.H.); Tel.: +86-0373-304-0418 (J.-C.W. & Y.H.)

Abstract: In this study, Cu and Cu₂O hybrid nanoparticles were synthesized onto the WO₃ nanoflake film using a one-step electrodeposition method. The critical advance is the use of a heterojunction consisting of WO₃ flakes and Cu₂O as an innovative stack design, thereby achieving excellent performance for CO₂ photoreduction with water vapor under visible light irradiation. Notably, with the modified Cu nanoparticles, the selectivity of CH₄ increased from nearly 0% to 96.7%, while that of CO fell down from 94.5% to 0%. The yields of CH₄, H₂ and O₂ reached 2.43, 0.32 and 3.45 mmol/g_{cat} after 24 h of visible light irradiation, respectively. The boosted photocatalytic performance primarily originated from effective charge-transfer in the heterojunction and acceleration of electron-proton transfer in the presence of Cu nanoparticles. The S-scheme charge transfer mode was further proposed by the in situ-XPS measurement. In this regard, the heterojunction construction showed great significance in the design of efficient catalysts for CO₂ photoreduction application.

Keywords: CO₂ reduction; selectivity; Cu/Cu₂O/WO₃; photocatalysis; S-scheme



Citation: Shi, W.; Wang, J.-C.; Chen, A.; Xu, X.; Wang, S.; Li, R.; Zhang, W.; Hou, Y. Cu Nanoparticles Modified Step-Scheme Cu₂O/WO₃ Heterojunction Nanoflakes for Visible-Light-Driven Conversion of CO₂ to CH₄. *Nanomaterials* **2022**, *12*, 2284. <https://doi.org/10.3390/nano12132284>

Academic Editor: Antonino Gulino

Received: 15 June 2022

Accepted: 30 June 2022

Published: 2 July 2022

Publisher's Note: MDPI stays neutral with regard to jurisdictional claims in published maps and institutional affiliations.



Copyright: © 2022 by the authors. Licensee MDPI, Basel, Switzerland. This article is an open access article distributed under the terms and conditions of the Creative Commons Attribution (CC BY) license (<https://creativecommons.org/licenses/by/4.0/>).

1. Introduction

The rapid growth of atmospheric carbon dioxide (CO₂) concentration has attracted considerable attention due to its greenhouse effect on the global climate [1,2]. Developing artificial photosynthesis routes by reducing anthropogenic CO₂ emissions using solar energy instead of carbon-based fuels such as methane, methanol or carbon monoxide is still an intensive research topic in the environmental and energy field [2–4]. Since a TiO₂ photocatalyst was used to reduce CO₂ into methanol and formaldehyde by Inoue et al. in 1972 [5], most semiconductor photocatalysts, such as g-C₃N₄, CeO₂, W₁₈O₄₉ and Bi₂WO₆ have received immense attention for CO₂ reduction under visible light irradiation, which occupies 44% of solar light [6–11]. Among the common photocatalysts, WO₃ material has gradually gained special scientific interest due to its relatively narrow bandgap (E_g~2.8 eV) and unique crystal structure containing a network of corner-shared octahedral units of [WO₆], which could theoretically utilize 12% of solar light and enhance charge migration in the catalyst [12]. Although WO₃ crystals exhibit various phases, few studies have focused on hexagonal phase WO₃ (*h*-WO₃) for photocatalytic CO₂ reduction [8,13,14]. *h*-WO₃ not only exhibits excellent visible light responsive properties according to its good photochromic ability [15], but also strong CO₂ adsorption at low-pressure due to the presence of ultramicro-sized tunnels [16]. It is thus considered as a potential visible-light-driven (VLD) photocatalyst for CO₂ reduction. However, the application of photocatalytic

CO₂ reduction for *h*-WO₃ is seriously hindered by poor charge separation and reduction ability [17,18].

It is well known that two-dimensional (2D) semiconductors exhibit superior solar-driven photocatalytic activity as a result of improved photoexcited charge separation, compared with that of bulk photocatalysts [19,20]. The 2D nanostructure also greatly influences the optical properties and electronic properties of semiconductors [21]. In particular, the travel distance of photoexcited carriers in the WO₃ nanoflake becomes short, and more photons can be adsorbed by the nanoflake in a remarkably short time under low photon flux density due to its large surface area [22]. It is thus considered that *h*-WO₃ nanoflakes could reduce charge recombination and improve the performance of photocatalytic CO₂ reduction. In addition, there have been few reports on the hydrothermal fabrication of nanostructured *h*-WO₃ photocatalysts [16,23,24], and the metastable hexagonal phase has limited its development and application [17,25]. Therefore, it is still a conceptual challenge in the field of materials research to fabricate heat-resisting *h*-WO₃ nanoflakes for CO₂ reduction. Apart from nanostructure engineering, heterojunction construction is also a prospective way of achieving improved redox abilities and efficient separation of photoexcited electrons and holes for *h*-WO₃ [2,26]. Among the numerous heterojunction photocatalysts, the heterostructured system with a staggered band alignment has drawn much attention due to its efficient charge separation [27]. Notably, the charge transfer (step-scheme mode) in the above junction directly quenches the weaker oxidative holes and reductive electrons, which is preferable to obtain photoexcited carriers with stronger redox abilities [28]. Recently, cuprous oxide (Cu₂O) with a conduction band of -1.15 eV (vs. NHE) has been utilized as a VLD semiconductor photocatalyst or co-catalyst for CO₂ reduction [29,30]. Nevertheless, Cu₂O exhibits weak oxidation ability and poor photostability. An effective way to address these issues may be coupling Cu₂O and WO₃ to construct a heterostructured system with a step-scheme (S-scheme) charge transportation mode. S-scheme systems consisting of monoclinic or orthorhombic WO₃ and Cu₂O were constructed for organic degradation, CO₂ reduction or photoelectrocatalytic water splitting [31–33]. To our best knowledge, there are few studies regarding hexagonal phase WO₃ nanoflakes and Cu₂O for photocatalytic CO₂ reduction under visible light irradiation.

Except for enhanced photocatalytic activity for CO₂ reduction, the selectivity of multiple hydrocarbon products plays a key role in their further application in the chemical industry. The influence of the specific surface structure of the photocatalyst cannot be ignored in the process of CO₂ reduction [34,35]. Due to the eight-electron reaction of CH₄ generation from CO₂, loading co-catalysts with fast electron transfer, including Au, Pt, Ag and Ti, could be conducive to control the reduction of products [35–38]. Non-noble-metal Cu co-catalyst has become a newly emerging research spot for CO₂ reduction. Albo et al. reported the deposition of Cu nanoparticles on the TiO₂ surface, which facilitated the photocatalytic process from CO₂ to CH₃OH [39]. Meng et al. proved that Cu co-catalyst played a pivotal role in increasing methane selectivity in the CO₂ photoreduction process for the S doped g-C₃N₄ catalyst [40]. In the Cu₂O/WO₃ system, loading Cu co-catalysts can originate from Cu₂O with unsaturated coordination sites dispersed on the surface of the catalyst, and offer more catalytic centers and act as the electron sink to increase the concentration of charge carriers. Therefore, the construction of a Cu/Cu₂O/WO₃ catalyst could accelerate charge separation across the Cu₂O/WO₃ heterojunction interface and modulate product selectivity for photocatalytic CO₂ reduction.

Herein, we report the synthesis of Cu and Cu₂O species onto WO₃ nanoflakes by a one-step electrodeposition method. The photocatalytic performances for CO₂ reduction with water vapor over the obtained samples were investigated under visible light irradiation ($\lambda > 400$ nm), and the influence of Cu nanoparticles on product selectivity was studied. The band structure of the heterojunction was measured and the S-scheme charge-transfer mode was further verified.

2. Materials and Methods

2.1. Materials Synthesis

WO₃ nanoflake film was synthesized by the solvothermal-calcination method. Before solvothermal growth, a thin seed layer was deposited onto the fluorine-doped tin oxide (FTO)-coated glass substrate (2.3 cm × 2.0 cm) by spin coating the precursor solution, which was made by dissolving 1.25 g of H₂WO₄ in 30 wt% H₂O₂ (8 mL), followed by annealing at 500 °C for 2 h in air. The H₂WO₄ solution for solvothermal treatment was prepared by dissolving 1.25 g of H₂WO₄ into 30 wt% H₂O₂ (15 mL) and heating at 95 °C for 2 h. Nanoflake growth was achieved using 3 mL of H₂WO₄ solution mixed with 0.5 mL of HCl (6 mol/L) and 12.5 mL of acetonitrile. A vertically oriented FTO-glass substrate was immersed into the above solution and placed within a Teflon lined stainless steel autoclave, which was then sealed and maintained at 180 °C for 3 h. The substrate was then rinsed with deionized water and dried in air. The WO₃ nanoflake film was obtained after annealing at 500 °C for 2 h in air.

The electrodeposition was performed in a standard three-electrode system. The FTO substrates (2.3 cm × 2.0 cm) were used as the working electrodes. The platinum sheet (1.0 cm × 1.0 cm × 0.2 cm) and Ag/AgCl electrode were used as the counter and reference electrodes, respectively. All of the chemicals were used without further purification. Before electrodeposition, the substrates were rinsed with distilled water and then cleaned by ultrasonic treatment in ethanol for 10 min. Cu₂O was electrodeposited in 0.02 mol/L Cu(OAc)₂ aqueous solution (50 mL) containing 0.02 mol/L acetic acid (5 mL) using chronopotentiometry at −0.4 V with 0.5 s for 150 cycles. The Cu/Cu₂O sample was obtained at −0.7 V under the similar conditions as above.

Cu₂O/WO₃ and Cu/Cu₂O/WO₃ films were synthesized by electrodeposition of Cu₂O and Cu/Cu₂O on the obtained WO₃ nanoflakes, respectively. Typically, the deposition process was conducted in Cu(OAc)₂ aqueous solution (0.02 mol/L, 50 mL) using chronopotentiometry electrodeposition with 0.5 s in 150 cycles, and the Cu₂O/WO₃ and Cu/Cu₂O/WO₃ films samples were obtained at −0.4 and −0.7 V, respectively. All the samples were then rinsed with deionized water and dried in air. Additionally, Cu₂O and Cu/Cu₂O films were prepared by the similar method, and Cu₂O and Cu/Cu₂O nanoparticles were broken off from the above samples by the ultrasound method. The dispersion solutions of Cu₂O and Cu/Cu₂O nanoparticles were then severally sprayed onto the WO₃ nanoflakes, and the obtained films were finally denoted as Cu₂O/WO₃ m and Cu/Cu₂O/WO₃ m samples.

2.2. Characterization

The crystal phases of the samples were recorded using an X-ray diffractometer (PANalytical X'pert PRO, Netherlands) with a Cu K α irradiation source ($\lambda = 0.154$ nm) and 0.15°/s scanning step. A scanning electron microscope (SEM, Nova NanoSEM 450, FEI) using the acceleration 300 kV voltage was used to characterize the morphology of the obtained products. Transmission electron microscopy (TEM) was obtained on a Tecnai G2 F20 S-TWIN electron microscope. Furthermore, high-resolution transmission electron microscopy (HRTEM) and Energy Dispersive X-ray spectroscopy (EDX) was employed and the corresponding fast Fourier transform (FFT) was evaluated by Gatan Digital Micro-graph software (Gatan Inc., Pleasanton, CA, USA). X-ray photoelectron spectroscopy (XPS) measurements were carried out at room temperature on a Thermo escalab 250Xi X-ray Photoelectron Spectrometer with a monochromatic Al K α radiation ($h\nu = 1486.6$ eV). For XPS analysis, the samples without exposure to air were dried in N₂ flow gas and vacuum packed to avoid any impurity. All spectra were calibrated to the C_{1s} peak at 284.6 eV. The peak position was estimated using a fitting procedure based on the summation of Lorentzian and Gaussian functions using the XPSPEAK 4.1 program. UV-Vis diffuse reflectance spectra (DRS) were performed on a scan UV-Vis spectrometer (Cary 5000). The composition for the composites was determined by ICP-AES analysis using Thermo Scientific iCAP 6000 spectrometry. The photoelectrochemical test was recorded in a conventional three-electrode system by a CHI 660E electrochemical

workstation (Chenhua, Shanghai, China). The photocurrents of the photocatalysts were measured at 0.0 V (vs. Ag/AgCl) in Na₂SO₄ aqueous solution after being purged by N₂ under UV-visible light with an AM 1.5 G filter.

2.3. Photocatalytic Performance Tests

Photocatalytic CO₂ reduction activity with gaseous phase H₂O was evaluated in a CEL-HPR100 stainless steel cylindrical vessel (Beijing China Education Au-Light Co., Ltd., China), and the light source was a PLS-SXE 300 Xenon arc lamp with a UV cutoff filter ($\lambda > 400$ nm). The compressed high purity CO₂ gas (99.995%) was passed across a deionized water bubbler, which generated a mixture of CO₂ and H₂O vapor. After visible-light irradiation, the product yields and types in the gas phase were analyzed using a GC-7890II gas chromatograph (Beijing China Education Au-Light Co., Ltd., China), and the hydrocarbon product was further analyzed by 7890A-5975C GC-MS (Agilent Technologies Inc., Santa Clara, CA, USA). The experimental process is detailed in Supplementary Material S1.

The product selectivity (S) for CO₂ reduction was calculated with the following Equations (1)–(3):

$$S_{\text{CO}} (\%) = 2 \times N_{\text{CO}} / (2 \times N_{\text{CO}} + 8 \times N_{\text{CH}_4} + 2 \times N_{\text{H}_2}) \times 100 \quad (1)$$

$$S_{\text{H}_2} (\%) = 2 \times N_{\text{H}_2} / (2 \times N_{\text{CO}} + 8 \times N_{\text{CH}_4} + 2 \times N_{\text{H}_2}) \times 100 \quad (2)$$

$$S_{\text{CH}_4} (\%) = 2 \times N_{\text{CH}_4} / (2 \times N_{\text{CO}} + 8 \times N_{\text{CH}_4} + 2 \times N_{\text{H}_2}) \times 100 \quad (3)$$

N_{CO} , N_{CH_4} and N_{H_2} were on behalf of the yield of detected CO, CH₄ and H₂ molecules in the photocatalytic process of CO₂ reduction with H₂O vapor.

3. Results and Discussion

3.1. Structure, Composition and Morphology

The XRD patterns of the as-prepared samples are presented in Figure 1. Several diffraction peaks at 13.9, 23.2, 27.2, 28.1, 47.4 and 49.8° (marked with black dotted lines) were observed corresponding to (1 0 0), (0 0 2), (1 0 2), (2 0 0), (0 0 4) and (2 2 0) planes of hexagonal WO₃ (PDF card No. 01-085-2460). This is because the percentage of exposed facets was estimated by the respective peak areas of the facets [41]. Hence, the WO₃ component in the bare and composite samples preferentially exposed (0 0 2) facets. Simultaneously, the diffraction peaks of Cu₂O sample (marked with green dotted lines) matched perfectly with those of cubic phase Cu₂O (PDF card No. 01-078-2076). To further explore the existence of Cu metal in the composite, the XRD pattern of Cu/Cu₂O sample was studied, avoiding interference from the diffraction peak of hexagonal WO₃, and the characteristic peaks at 43.4 and 50.6° (marked with pink dotted lines) were attributed to metallic Cu (PDF card No. 03-065-9743). Moreover, Cu metal was proven to be present in the Cu/Cu₂O/WO₃ composite. As a result, Cu and Cu₂O were simultaneously electrodeposited onto hexagonal WO₃, indicating the successful construction of the Cu/Cu₂O/WO₃ composite.

X-ray photoelectron spectroscopy (XPS) measurements were carried out to elucidate the surface composition and chemical states of the elements. The survey XPS spectrum of the typical Cu/Cu₂O/WO₃ sample indicated that the composite mainly consisted of W, Cu and O electrons. To gain further insight into the chemical bonding between W and other atoms in the composite, the high resolution XPS spectrum of W 4f (Figure 2a) was deconvoluted by Gaussian-Lorentzian analysis. The peaks at binding energies of 37.7 and 35.7 eV were ascribed to W (VI) state in tungsten oxide materials, while two distinct peaks at 34.5 and 36.4 eV were consistent with the values of W (V) oxidation state for all the samples [42,43]. The existence of W (V) was necessary to maintain the opening structure of hexagonal WO₃ [14]. However, the area ratios of W (V) and W (VI) in the composite were higher than those of the bare WO₃ sample (Table S1) due to the electroreduction process for Cu₂O deposition. In the high-resolution Cu 2p XPS spectrum (Figure 2b), two conspicuous peaks were observed at binding energies of 952.3 eV for Cu (I) 2p_{1/2} and 932.5 eV for Cu(I) 2p_{3/2} [44]. Furthermore, the Cu and W diffraction peaks of the composite shifted slightly

compared with those of pure samples, which was the reason that the intense interaction existed between WO_3 and Cu_2O component in the composites, implying the formation of heterojunction. Cu LMM Auger spectra (Figure 2c) were further performed to explore the chemical state of the Cu element, The Auger parameter can be calculated from the equation of $\alpha' = E_k$ (Auger electron) + E_b (photoelectron). Here, E_k is the kinetic energy, and E_b is the binding energy. The Auger parameter values of the Cu (I) and Cu (0) in the Cu/ Cu_2O / WO_3 composite were determined to be 1848.7 and 1851.2 eV, respectively, which indicated the existence of Cu (I) and Cu (0) in the Cu/ Cu_2O / WO_3 sample [45,46].

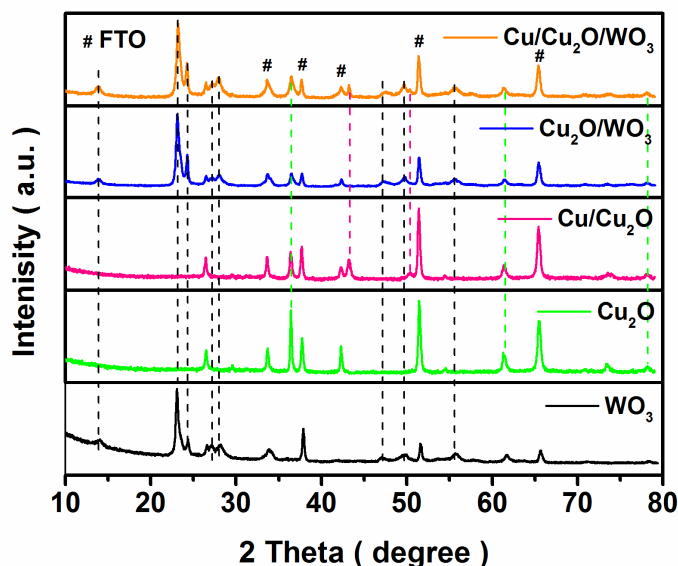


Figure 1. XRD patterns of the bare and composite samples (# sign: the characteristic peak of FTO substrate).

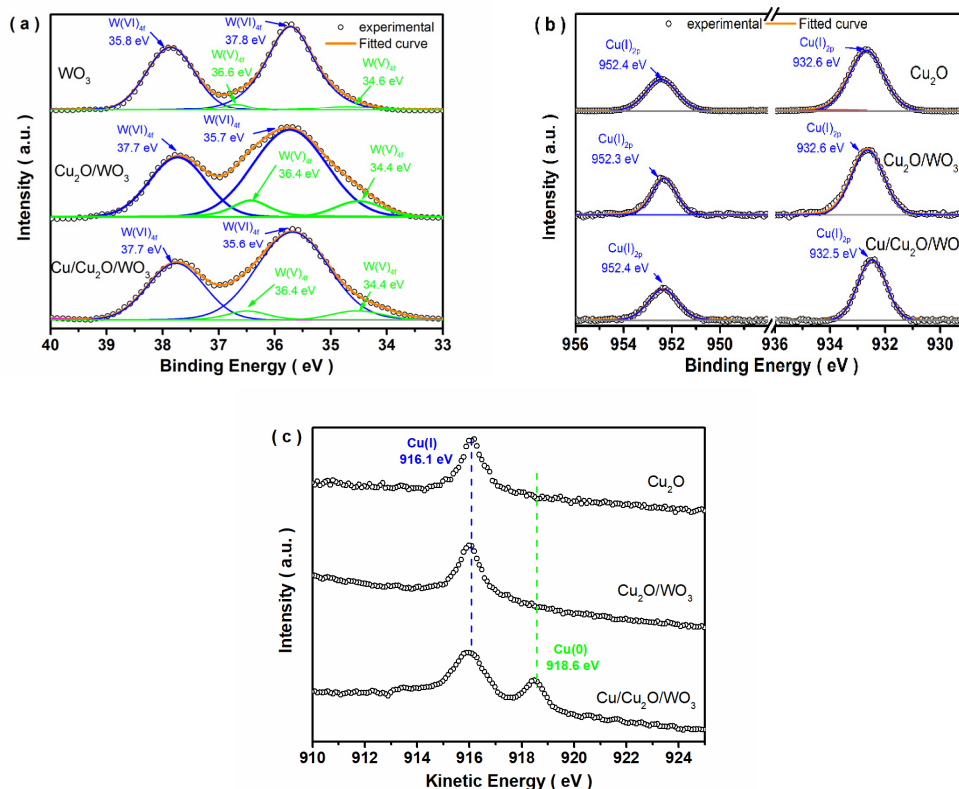


Figure 2. XPS spectra (a): W 4f, (b): Cu 2p, and Cu LMM Auger spectra (c) of the obtained samples.

The morphologies of the as-obtained WO_3 , $\text{Cu}_2\text{O}/\text{WO}_3$ and $\text{Cu}/\text{Cu}_2\text{O}/\text{WO}_3$ powders were visualized using SEM images. As shown in Figure 3, all the samples exhibited the typical sheet morphology with various sizes. Furthermore, the SEM image in Figure 3a showed that the nanoflake surface was rough and porous. As shown in Figure 3b,c, both of the composites kept uniform sheet morphology, and the sheet thicknesses after electrodeposition of Cu_2O and $\text{Cu}/\text{Cu}_2\text{O}$ had no obvious changes compared with that of bare WO_3 . Although there was no obvious difference in Cu content between $\text{Cu}_2\text{O}/\text{WO}_3$ and $\text{Cu}/\text{Cu}_2\text{O}/\text{WO}_3$ according to the ICP-AES analysis (Table S2), the nanoflake surface of $\text{Cu}/\text{Cu}_2\text{O}/\text{WO}_3$ exhibited distinct embossment (Figure 3c).

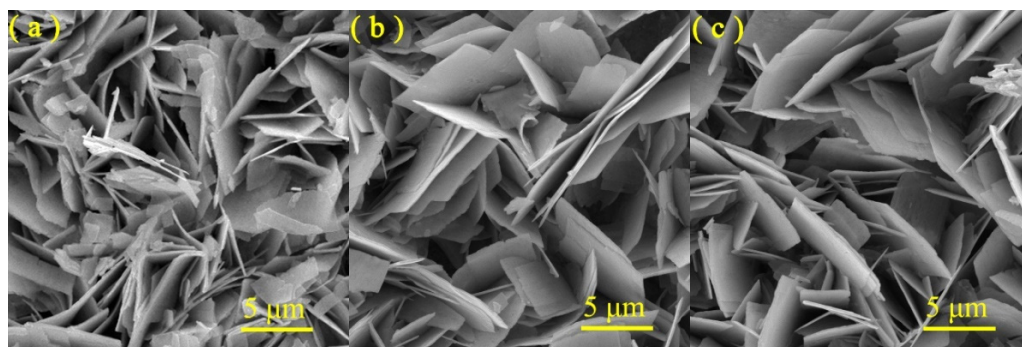


Figure 3. SEM images of WO_3 (a), $\text{Cu}_2\text{O}/\text{WO}_3$ (b) and $\text{Cu}/\text{Cu}_2\text{O}/\text{WO}_3$ (c) samples.

Micro-structures of the obtained samples were investigated by TEM observation. Figure 4 revealed that the typical nanoflake-like morphology was observed with a sharp edge and clean boundary. In Figure 4a, the WO_3 nanoflake had a porous surface morphology. The fringe spacings of 0.634 and 0.366 nm were discovered (inset of Figure 4a), which were consistent with the (1 0 0) and (0 0 2) lattice planes of hexagonal WO_3 , respectively. In Figure 4b, $\text{Cu}_2\text{O}/\text{WO}_3$ still kept a nanoflake-like morphology with smaller porous sizes compared with that of WO_3 . The lattice fringes with spacings of 0.246 and 0.213 nm were distinctly found (inset of Figure 4b) corresponding to the (1 1 1) and (2 0 0) planes of cubic Cu_2O . Similar nanoflake-like morphology was observed for the $\text{Cu}/\text{Cu}_2\text{O}/\text{WO}_3$ sample in Figure 4c, and the (2 0 0) crystal facet of metallic Cu with lattice spacing of 0.180 nm was observed, except for the crystal facet of Cu_2O (top-right inset of Figure 4c). Furthermore, the scattered Cu nanoparticles around the $\text{Cu}/\text{Cu}_2\text{O}/\text{WO}_3$ nanoflake by ultrasonic exfoliation were observed with clear lattice fringes of 0.180 and 0.208 nm were observed around the nanoflake (bottom-left inset of Figure 4c), and the size distribution of Cu nanoparticles in the selected area (framed in red, corresponding enlarged view in Figure S1) obeyed a logical normal distribution with an average diameter of 5.6 ± 1.1 nm (Figure S2). According to the elemental mapping images in Figure 4d, W, Cu and O elements were uniformly distributed in the $\text{Cu}/\text{Cu}_2\text{O}/\text{WO}_3$ sample, and the Cu element appeared on the surface, as well as around the nanoflakes. The above results demonstrate that Cu_2O was uniformly electrodeposited on the surface of the WO_3 nanoflake, and metallic Cu also existed in the $\text{Cu}/\text{Cu}_2\text{O}/\text{WO}_3$ sample.

The light absorption property is crucial for the utilization efficiency of solar energy for the catalyst. According to the UV-Vis diffuse reflectance spectra (Figure 5), all the composites showed strong absorption in the visible light region, indicating the feasibility of utilizing visible light for CO_2 photoreduction. The band gaps (E_g) of the samples were estimated by the plots of $(\alpha h\nu)^2$ versus photo energy ($h\nu$) (Figure S3 and Table S2), and the calculated E_g values of WO_3 and Cu_2O were 2.86 and 2.05 eV, respectively.

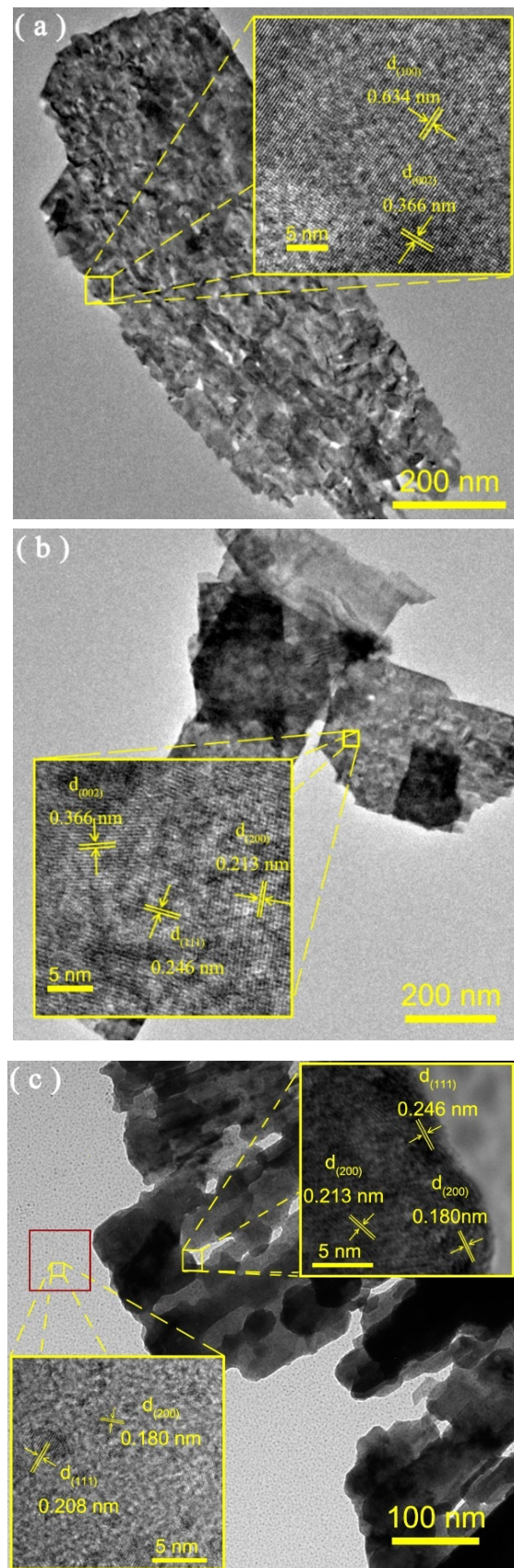


Figure 4. Cont.

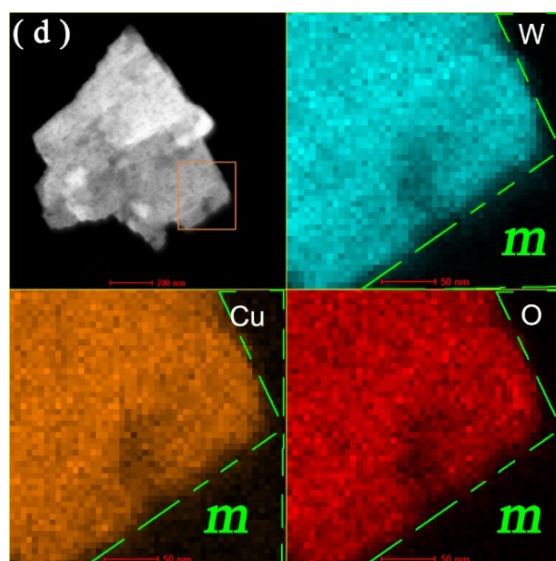


Figure 4. TEM images of WO_3 (a), $\text{Cu}_2\text{O}/\text{WO}_3$ (b) and $\text{Cu}/\text{Cu}_2\text{O}/\text{WO}_3$ (c), inset: HRTEM images), and elemental mapping images of $\text{Cu}/\text{Cu}_2\text{O}/\text{WO}_3$ (d).

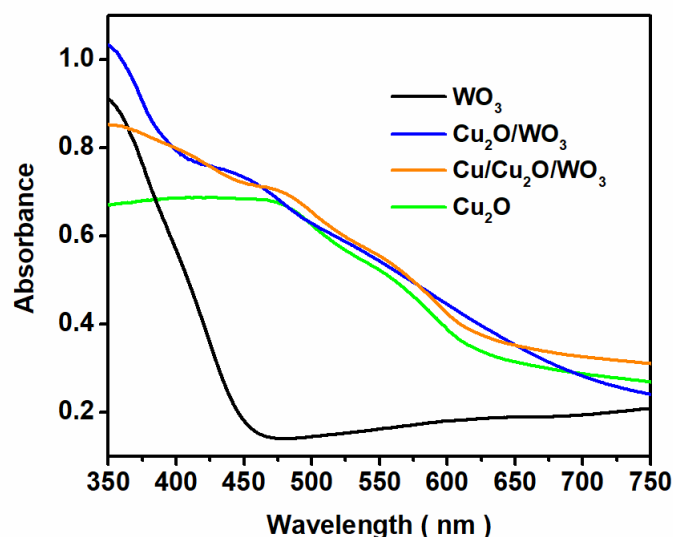


Figure 5. UV-Vis diffuse reflectance spectra of WO_3 , Cu_2O , $\text{Cu}_2\text{O}/\text{WO}_3$ and $\text{Cu}/\text{Cu}_2\text{O}/\text{WO}_3$ composites.

3.2. Photocatalytic Performance of CO_2 Reduction

The photocatalytic CO_2 reduction experiments were carried out under visible-light irradiation (>400 nm) for the as-prepared catalysts. The photocatalytic performances of CO_2 reduction with water vapor in Figure 6a showed that no products were generated over the WO_3 , Cu_2O and $\text{Cu}/\text{Cu}_2\text{O}$ samples. Conversely, CO , CH_4 , O_2 and H_2 products were obtained for the $\text{Cu}/\text{Cu}_2\text{O}/\text{WO}_3$ and $\text{Cu}_2\text{O}/\text{WO}_3$ composites, and no other products such as HCHO or CH_3OH were detected by either GC or GC-MS analyses. Furthermore, the product yields decreased for the mechanically dispersed $\text{Cu}_2\text{O}/\text{WO}_3$ m sample compared with those of the $\text{Cu}_2\text{O}/\text{WO}_3$, indicating that the loosely contacted interface was insufficient for photocatalytic CO_2 reduction. Additionally, the product selectivity for CO_2 reduction was analyzed for the $\text{Cu}/\text{Cu}_2\text{O}/\text{WO}_3$ and $\text{Cu}_2\text{O}/\text{WO}_3$ catalyst. Typically, the S_{CH_4} and S_{CO} values of $\text{Cu}_2\text{O}/\text{WO}_3$ were calculated to be about 0.1% and 94.5%, which demonstrated that CO_2 reactant was thermodynamically favorable to form CO by the two-electron reduction pathway. However, the S_{CH_4} and S_{CO} values of $\text{Cu}/\text{Cu}_2\text{O}/\text{WO}_3$ were calculated to be 96.7% and 0.0%, indicating that the metallic Cu promoted the formation and utilization of proton-assisted multi-electrons pathway in the photocatalytic CO_2 reduction process [47]. The

CH₄, CO and O₂ yields for CO₂ photoreduction reached 1.87, 0.0065 and 2.63 mmol/g_{cat}, respectively. Compared with the photocatalytic activity of the reported catalysts (Table S3), the maximum rate of CH₄ product over Cu/Cu₂O/WO₃ was obviously higher and high product selectivity was also obtained. To explore the influence of loading Cu on the photocatalytic performance, the controlled experiments in different atmospheres were further investigated (Figure 6b). In the CO/H₂O atmosphere, more CH₄ molecules were produced over Cu/Cu₂O/WO₃ compared with that of Cu₂O/WO₃. Meanwhile, in the N₂/H₂O atmosphere, the H₂ yield from water splitting was improved with the existence of Cu in the composite, which indicated that Cu nanoparticles promoted the electron transfer and proton aggregation on the catalyst surface, improving the hydrogenated process for CO₂ reduction over the Cu/Cu₂O/WO₃ catalyst. The yields of products for the Cu/Cu₂O/WO₃ composite were further investigated in the CO₂/H₂O atmosphere within 24 h of irradiation. As shown in Figure 6c, the total yields of CH₄, H₂ and O₂ were enhanced with prolonging the irradiation time. The maximal yield rate of H₂ reached 0.013 mmol/g_{cat}/h at 24 h, and those of CH₄ and O₂ at 18 h were found to be 0.104 and 0.147 mmol/g_{cat}/h, respectively. The decreased yields of the photocatalytic CO₂ reduction were possibly due to oxidation of the formed carbonous compounds on the photocatalyst surface or the coverage of active sites by intermediates. Reproducibility and durability are critical for the long-term use of a catalyst in practical application. The results in Figure 6d show that the yields of CH₄ and H₂ for the typical Cu/Cu₂O/WO₃ catalyst slightly decreased, and the O₂ yield obviously fell down after 5 cycles. Notably, after the 5th cycling experiment, the photocatalyst was regenerated by the electro-reduction method at 0.05 V in 0.5 M Na₂SO₄ solution. In the 6th cycling experiment, all the yields were obviously promoted, which were similar to those of the fresh catalyst. To illustrate the stability of the Cu/Cu₂O/WO₃ catalyst, XPS measurements were conducted to investigate the change in chemical composition after the 5th cycle. As shown in the Cu 2p and W 4f XPS spectra (Figure S4), Cu (II) and W (V) were identified, which were probably derived from the oxidation of Cu (I) and reduction in W (VI), and W (V) possibly became the high recombination center of the photogenerated electrons and holes, leading to a slight decrease in the photocatalytic activity for CO₂ reduction.

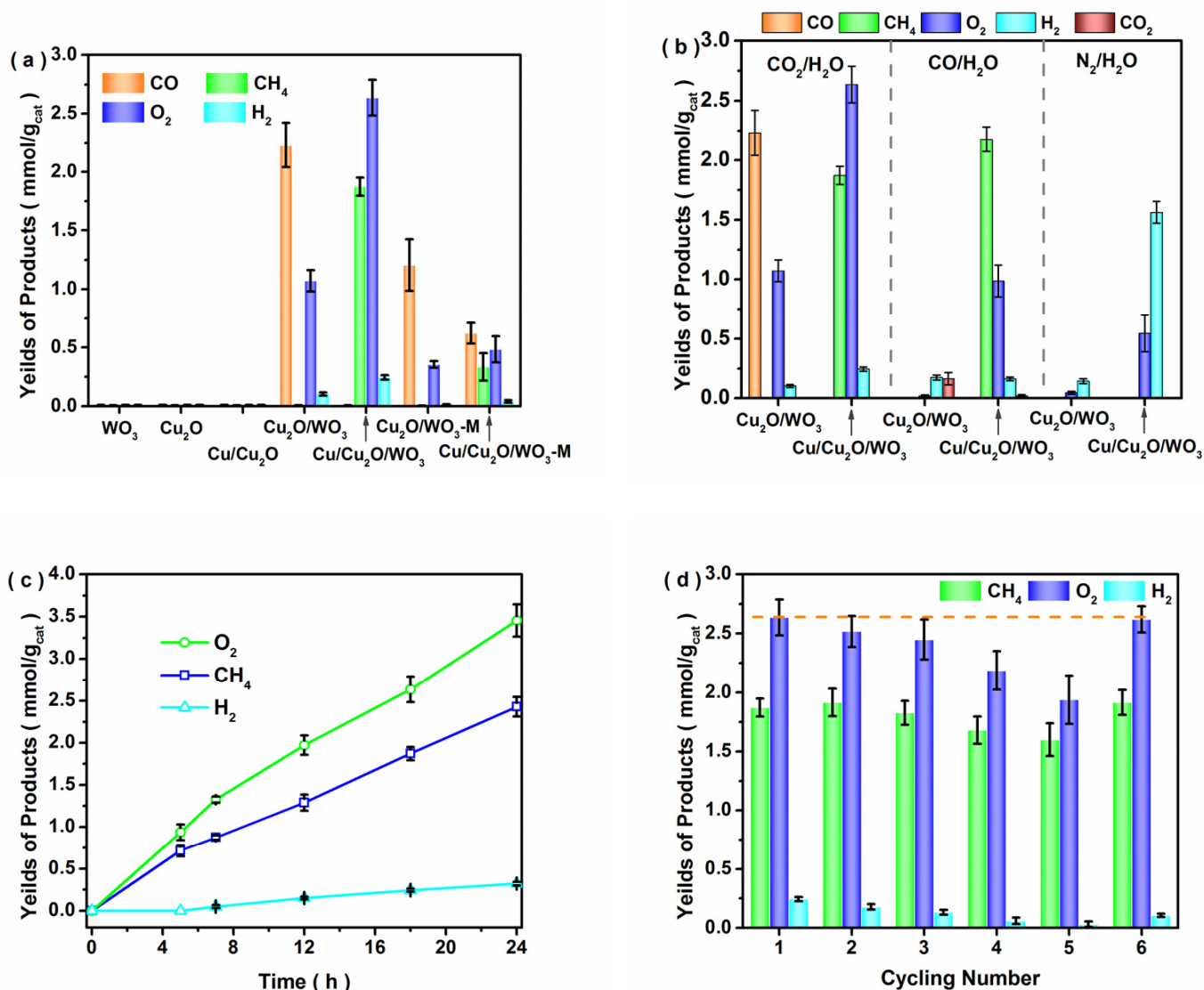


Figure 6. Photocatalytic performances of CO₂ reduction with water vapor after 18 h of visible light irradiation (>400 nm) over different samples (a), photocatalytic activities under different atmospheres (b), the yields of products for the Cu/Cu₂O/WO₃ composite in the CO₂/H₂O atmosphere within 24 h of irradiation (c) and product yields for the Cu/Cu₂O/WO₃ catalyst in cycling experiment under visible light irradiation for 18 h (d).

3.3. Possible Photocatalytic Mechanism

Transient photocurrent response and photoluminescence spectra were measured to investigate the charge separation. Based on the photo-electric properties during several on-off illumination cycles (Figure 7a), the photocurrent density of Cu₂O/WO₃ was higher than those of the bare WO₃ and Cu₂O samples, and the Cu/Cu₂O/WO₃ sample exhibited the highest photo-induced density among them. Moreover, the photoluminescence spectra of the photocatalysts at the excitation wavelength of 405 nm are present in Figure 7b, and the emission intensity of the Cu/Cu₂O/WO₃ composite distinctly decreased compared with those of the WO₃, Cu₂O and Cu₂O/WO₃ samples. The above results indicate the promoted separation of photogenerated electron-hole pairs in the Cu/Cu₂O/WO₃ composite.

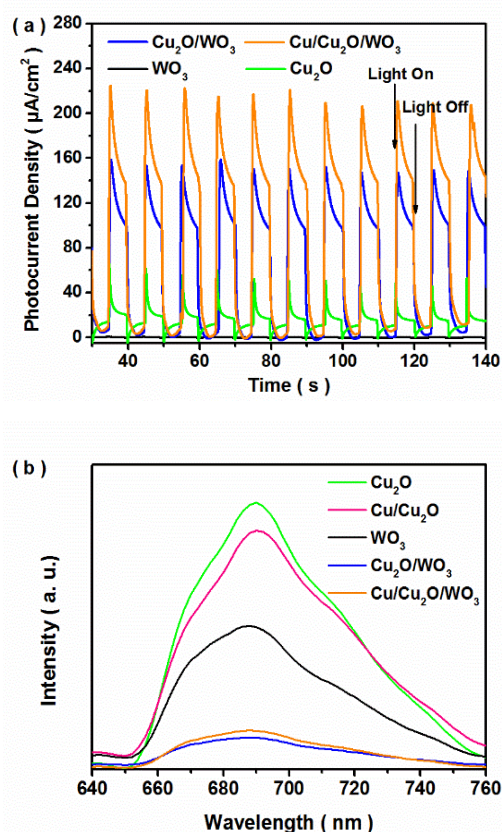


Figure 7. Photocurrent density (a) and photoluminescence spectra (b) of the obtained samples.

The band edge position and charge transport mode in the composite directly influenced the separation and redox ability of photoexcited charge carriers. Ultraviolet photoelectron spectra combined with E_g analysis were used to determine the electronic band structure of the catalyst. Figure 8a shows the UPS spectra of Cu₂O and WO₃. On the basis of the linear intersection method [48], the valence band (VB) of WO₃ was estimated to be -7.33 eV (vs. vacuum), and the conduction band (CB) was -4.47 eV (vs. vacuum) based on the E_g value of WO₃. According to the connection between vacuum energy and normal electrode potential (NHE) [29], the corresponding VB and CB positions of WO₃ were 2.89 and 0.03 eV (vs. NHE), respectively. Similarly, the VB and CB values of Cu₂O were separately calculated to be 0.91 and -1.14 eV (vs. NHE), which agreed well with previously reported results [31,49]. Hence, the heterostructure with staggered band alignment was successfully formed in this Cu₂O/WO₃ system, assuming that the possible band bending of the semiconductor was neglected. Based on the band energy structure of WO₃ and Cu₂O, two possible mechanisms for photo-induced carriers were proposed and described in Figure 8b,c. If the photo-excited charge carriers transferred according to the traditional model (Figure 8b), the photo-excited holes in the VB of WO₃ would transfer to the VB of Cu₂O, and the photo-excited electrons in the CB of Cu₂O would migrate to the CB of WO₃, where the accumulated electrons would not reduce CO₂ to CO/CH₄ or produce H₂ from H₂O on account of the more positive CB edge potential (0.21 eV vs. NHE) than the standard CO₂ reduction potential [4]. Similarly, the accumulated holes in Cu₂O would not accomplish H₂O oxidation due to the more negative VB of Cu₂O. Hence, the hypothesis of the traditional double-transfer model was invalid. The S-scheme charge transfer mode (Figure 8c) was proposed according to the enhanced photocatalytic activity of Cu/Cu₂O/WO₃. To verify the S-scheme charge transfer mode in this heterojunction, the XPS spectra of Cu₂O/WO₃ were measured in light and the results were shown in Figure 8d,e. The CB of Cu₂O and WO₃ were composed of Cu and W orbitals, respectively. Four peaks of W 4f in light shifted to a higher binding energy compared with these in

the dark. Simultaneously, two peaks of Cu 2p in light reversely shifted. It was implied that the photo-induced electrons transferred from WO₃ component to Cu₂O component in this heterojunction [50,51]. Specifically, the photoexcited holes in the VB of Cu₂O would transfer to WO₃ and recombine with the photoexcited electrons in the CB of WO₃. The CB potential of Cu₂O and VB potential of WO₃ thermodynamically realized photocatalytic CO₂ reduction and H₂O oxidation, respectively, and the metallic Cu co-catalyst facilitated the reduction process dynamically.

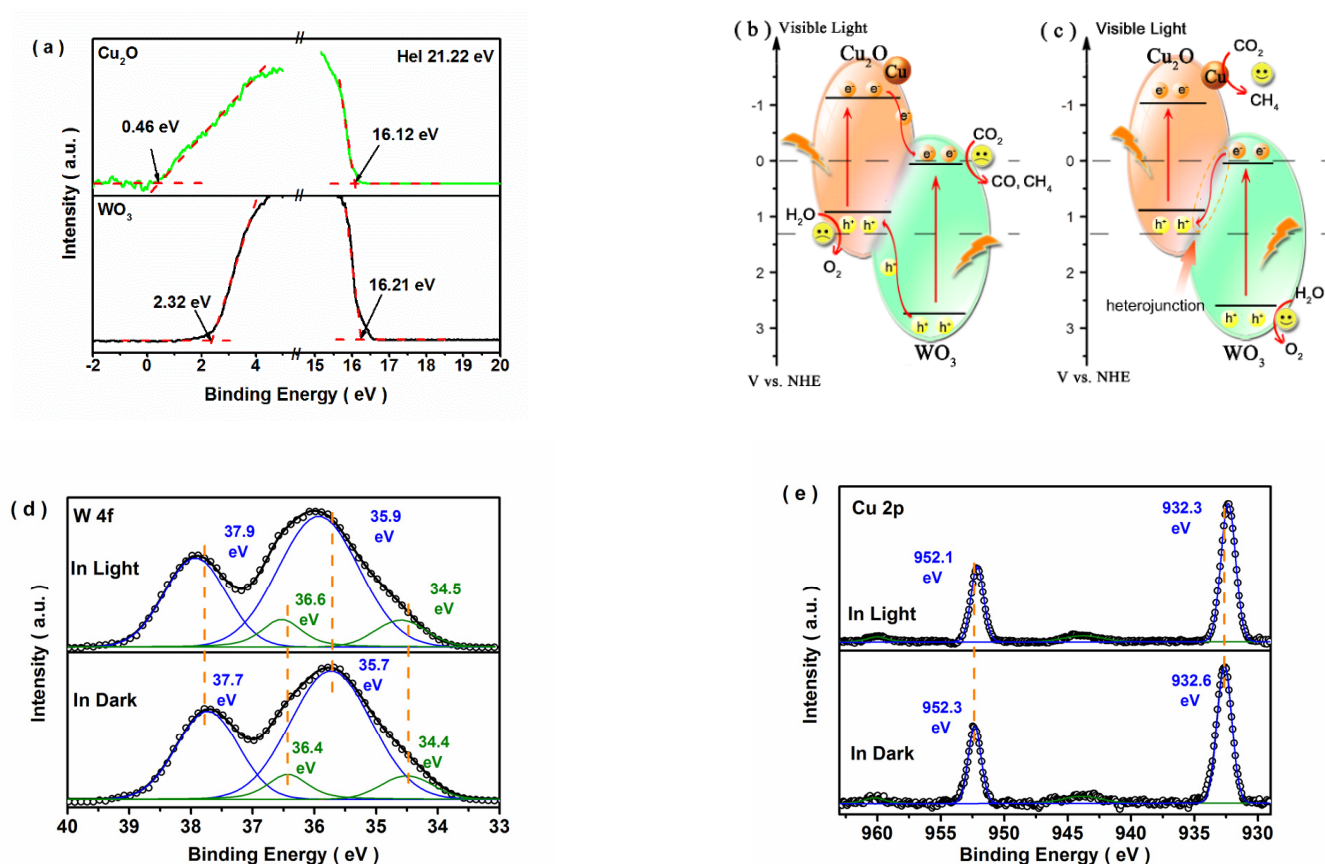


Figure 8. Ultraviolet photoelectron spectra of Cu₂O and WO₃ samples measured at the basics of -8 V (a), photocatalytic electron transfer modes of the Cu/Cu₂O/WO₃ composite: the traditional double transfer mode (b) and the S-scheme charge transfer mode (c), and XPS spectra of W 4f (d) and Cu 2p (e) for Cu₂O/WO₃ heterojunction in dark/light.

4. Conclusions

In summary, Cu and Cu/Cu₂O species were synthesized on the hexagonal WO₃ nanoflake films by the one-step electrodeposition method for photocatalytic CO₂ reduction with water vapor. The obtained Cu/Cu₂O/WO₃ catalyst exhibited excellent photocatalytic performance under visible light irradiation ($\lambda > 400$ nm) due to the construction of heterojunction, and the CH₄, H₂ and O₂ yields reached 2.43, 0.32 and 3.45 mmol/g_{cat} after 24 h of illumination, respectively. Notably, CH₄ molecules were generated as the major product over the Cu/Cu₂O/WO₃ catalyst, whereas Cu₂O/WO₃ facilitated CO generation. Efficient CH₄ formation for the Cu/Cu₂O/WO₃ catalyst was attributed to the modification of Cu nanoparticles favoring electron–proton transfer from CO to CH₄. The decreased photocatalytic activity in the cycling experiment was recovered by the regenerated treatment via electro reduction, removing the superfluous W(V) in the composite. Additionally, the S-scheme charge transfer mode and potential mechanism of CO₂ reduction were proposed by the results of XPS measurement and photocatalytic performance under light illumination with a specific wavelength. The present research may provide a promising strategy to

design ternary nanocomposite VLD photocatalysts and inspire further interest in tuning product selectivity for photocatalytic CO₂ conversion.

Supplementary Materials: The following supporting information can be downloaded at: <https://www.mdpi.com/article/10.3390/nano12132284/s1>, S1. Catalytic Experiment for CO₂ photoreduction; Table S1. ICP-AES analysis of Cu₂O/WO₃ and Cu/Cu₂O/WO₃ samples; Table S2. Band gaps of pure WO₃, Cu₂O, Cu₂O/WO₃ and Cu/Cu₂O/WO₃ samples; Table S3. Comparison of performance CO₂ conversion of the obtained material with other reported catalysts. Figure S1. TEM image of Cu nanoparticles in Cu/Cu₂O/WO₃ sample; Figure S2. Size distribution histogram of Cu nanoparticles.; Figure S3. The curves of $(\alpha h\nu)^2$ versus photo energy ($h\nu$); Figure S4. XPS spectra of Cu/Cu₂O/WO₃ in the cycling tests.

Author Contributions: Conceptualization, W.S., A.C. and J.-C.W.; software, X.X. and S.W.; validation, J.-C.W. and Y.H.; formal analysis, R.L. W.Z. and J.-C.W.; investigation, W.S.; resources, J.-C.W., R.L., W.Z. and Y.H.; data curation, J.-C.W.; writing—original draft preparation, X.X. and J.-C.W.; writing—review and editing, S.W.; supervision, W.S. and J.-C.W.; project administration, W.S. and J.-C.W.; funding acquisition, J.-C.W., R.L., W.Z. and Y.H. All authors have read and agreed to the published version of the manuscript.

Funding: This research was funded by the financial supports of National Natural Science Foundation of China (No. 51802082 and 51903073), Natural Science Foundation of Henan Province (No. 212300410221), Program for Science & Technology Innovation Talents in Universities of Henan Province (No. 21HATIT016), Key Scientific Research Project of Colleges and Universities in Henan Province (No. 21A430030), Key Scientific and Technological Project of Henan Province (No. 222102320100), National College Student Innovation and Entrepreneurship Training (No. 202110467024) and “Climbing” Project of Henan Institute of Science and Technology (No. 2018CG04).

Data Availability Statement: Data are contained within the article.

Conflicts of Interest: The authors declare no conflict of interest.

References

1. Wang, K.; Wang, T.; Islam, Q.A.; Wu, Y. Layered double hydroxide photocatalysts for solar fuel production. *Chin. J. Catal.* **2021**, *42*, 1944–1975. [[CrossRef](#)]
2. Wang, H.N.; Zou, Y.H.; Sun, H.X.; Chen, Y.; Li, S.L.; Lan, Y.Q. Recent progress and perspectives in heterogeneous photocatalytic CO₂ reduction through a solid-gas mode. *Coord. Chem. Rev.* **2021**, *438*, 213906. [[CrossRef](#)]
3. Wang, B.; Liu, J.W.; Yao, S.; Liu, F.Y.; Li, Y.K.; He, J.Q.; Lin, Z.; Huang, F.; Liu, C.; Wang, M.Y. Vacancy engineering in nanostructured semiconductors for enhancing photocatalysis. *J. Mater. Chem. A* **2021**, *9*, 17143–17172. [[CrossRef](#)]
4. Navarro-Jaen, S.; Virginie, M.; Bonin, J.; Robert, M.; Wojcieszak, R.; Khodakov, A.Y. Highlights and challenges in the selective reduction of carbon dioxide to methanol. *Nat. Rev. Chem.* **2021**, *5*, 564–579. [[CrossRef](#)]
5. Inoue, T.; Fujishima, A.; Konishi, S.; Honda, K. Photoelectrocatalytic reduction of carbon dioxide in aqueous suspensions of semiconductor powders. *Nature* **1979**, *277*, 637–638. [[CrossRef](#)]
6. Lu, Q.Q.; Eid, K.; Li, W.P.; Li, W.; Abdullah, A.M.; Xu, G.B.; Varma, R.S. Engineering graphitic carbon nitride (g-C₃N₄) for catalytic reduction of CO₂ to fuels and chemicals: Strategy and mechanism. *Green Chem.* **2021**, *23*, 5394–5428. [[CrossRef](#)]
7. Hezam, A.; Namratha, K.; Drmash, Q.A.; Ponnamm, D.; Wang, J.; Prasad, S.; Ahamed, M.; Cheng, C.; Byrappa, K. CeO₂ nanostructures enriched with oxygen vacancies for photocatalytic CO₂ reduction. *ACS Appl. Energy Mater.* **2020**, *3*, 138–148. [[CrossRef](#)]
8. Zhang, M.; Cheng, G.; Wei, Y.; Wen, Z.; Chen, R.; Xiong, J.; Li, W.; Han, C.; Li, Z. Cuprous ion (Cu⁺) doping induced surface/interface engineering for enhancing the CO₂ photoreduction capability of W₁₈O₄₉ nanowires. *J. Colloid Interface Sci.* **2020**, *572*, 306–317. [[CrossRef](#)]
9. Liu, Y.; Shen, D.; Zhang, Q.; Lin, Y.; Peng, F. Enhanced photocatalytic CO₂ reduction in H₂O vapor by atomically thin Bi₂WO₆ nanosheets with hydrophobic and nonpolar surface. *Appl. Catal. B* **2021**, *283*, 119630. [[CrossRef](#)]
10. Chen, D.; Zhang, X.; Lee, A.F. Synthetic strategies to nanostructured photocatalysts for CO₂ reduction to solar fuels and chemicals. *J. Mater. Chem. A* **2015**, *3*, 14487–14516. [[CrossRef](#)]
11. Zhao, G.; Huang, X.; Wang, X.; Wang, X. Progress in catalyst exploration for heterogeneous CO₂ reduction and utilization: A critical review. *J. Mater. Chem. A* **2017**, *5*, 21625–21649. [[CrossRef](#)]
12. Wang, H.; Zhang, L.; Wang, K.; Sun, X.; Wang, W. Enhanced photocatalytic CO₂ reduction to methane over WO₃·0.33H₂O via Mo doping. *Appl. Catal. B* **2019**, *243*, 771–779. [[CrossRef](#)]
13. Xie, Y.P.; Liu, G.; Yin, L.; Cheng, H.M. Crystal facet-dependent photocatalytic oxidation and reduction reactivity of monoclinic WO₃ for solar energy conversion. *J. Mater. Chem.* **2012**, *22*, 6746–6751. [[CrossRef](#)]

14. Tian, F.H.; Zhao, L.; Xue, X.-Y.; Shen, Y.; Jia, X.; Chen, S.; Wang, Z. DFT study of CO sensing mechanism on hexagonal WO₃ (0 0 1) surface: The role of oxygen vacancy. *Appl. Surf. Sci.* **2014**, *311*, 362–368. [[CrossRef](#)]
15. Li, N.; Zhao, Y.; Wang, Y.; Lu, Y.; Song, Y.; Huang, Z.; Li, Y.; Zhao, J. Aqueous synthesis and visible-light photochromism of metastable-WO₃ hierarchical nanostructures. *Eur. J. Inorg. Chem.* **2015**, *17*, 2804–2812. [[CrossRef](#)]
16. Sun, W.; Yeung, M.T.; Lech, A.T.; Lin, C.-W.; Lee, C.; Li, T.; Duan, X.; Zhou, J.; Kanar, R.B. High surface area tunnels in hexagonal WO₃. *Nano Lett.* **2015**, *15*, 4834–4838. [[CrossRef](#)]
17. Dong, P.; Hou, G.; Xi, X.; Shao, R.; Dong, F. WO₃-based photocatalysts: Morphology control, activity enhancement and multifunctional applications. *Environ. Sci. Nano* **2017**, *4*, 539–557. [[CrossRef](#)]
18. Yang, G.; Zhu, X.; Cheng, G.; Chen, R.; Xiong, J.; Li, W.; Li, Y. Engineered tungsten oxide-based photocatalysts for CO₂ reduction: Categories and roles. *J. Mater. Chem. A* **2021**, *9*, 22781–22809. [[CrossRef](#)]
19. Babu, V.J.; Vempati, S.; Uyar, T.; Ramakrishna, S. Review of one-dimensional and two-dimensional nanostructured materials for hydrogen generation. *Phys. Chem. Chem. Phys.* **2015**, *17*, 2960–2986. [[CrossRef](#)]
20. Chen, W.; Hou, X.; Shi, X.; Pan, H. Two-dimensional Janus transition metal oxides and chalcogenides: Multifunctional properties for photocatalysts, electronics. *ACS Appl. Mater. Interfaces* **2018**, *10*, 35289–35295. [[CrossRef](#)]
21. Sumesh, C.K.; Peter, S.C. Two-dimensional semiconductor transition metal based chalcogenide based heterostructures for water splitting applications. *Dalton Trans.* **2019**, *48*, 12772–12802. [[CrossRef](#)] [[PubMed](#)]
22. Hao, S.; Zhao, X.; Cheng, Q.; Xing, Y.; Ma, W.; Wang, X.; Zhao, G.; Xu, X. A mini review of the preparation and photocatalytic properties of two-dimensional materials. *Front. Chem.* **2020**, *8*, 582146. [[CrossRef](#)] [[PubMed](#)]
23. Wang, X.; Zhang, H.; Liu, L.; Li, W.; Cao, P. Controlled morphologies and growth direction of WO₃ nanostructures hydrothermally synthesized with citric acid. *Mater. Lett.* **2014**, *130*, 248–251. [[CrossRef](#)]
24. Peng, T.; Ke, D.; Xiao, J.; Wang, L.; Hu, J.; Zan, L. Hexagonal phase WO₃ nanorods: Hydrothermal preparation, formation mechanism and its photocatalytic O₂ production under visible-light irradiation. *J. Solid State Chem.* **2012**, *194*, 250–256. [[CrossRef](#)]
25. Zheng, G.; Wang, J.; Liu, H.; Murugadoss, V.; Zu, G.; Che, H.; Lai, C.; Li, H.; Ding, T.; Gao, Q.; et al. Tungsten oxide nanostructures and nanocomposites for photoelectrochemical water splitting. *Nanoscale* **2019**, *11*, 18968–18994. [[CrossRef](#)]
26. Lin, N.; Lin, Y.; Qian, X.; Wang, X.; Su, W. Construction of a 2D/2D WO₃/LaTiO₂N Direct Z-scheme photocatalyst for enhanced CO₂ reduction performance under visible light. *ACS Sustain. Chem. Eng.* **2021**, *9*, 13686–13694. [[CrossRef](#)]
27. Moniz, S.J.A.; Shevlin, S.; Martin, D.; Guo, Z.X.; Tang, J.J. Visible-light driven heterojunction photocatalysts for water splitting—a critical review. *Energy Environ. Sci.* **2015**, *8*, 731–759. [[CrossRef](#)]
28. Xu, Q.; Zhang, L.; Cheng, B.; Fan, J.; Yu, J. S-scheme heterojunction photocatalyst. *Chem* **2020**, *6*, 1543–1559. [[CrossRef](#)]
29. Wang, J.-C.; Zhang, L.; Fang, W.-X.; Ren, J.; Li, Y.-Y.; Yao, H.-C.; Wang, J.-S.; Li, Z.-J. Enhanced photoreduction CO₂ activity over direct Z-scheme alpha-Fe₂O₃/Cu₂O heterostructures under visible light irradiation. *ACS Appl. Mater. Interfaces* **2015**, *16*, 8631–8639. [[CrossRef](#)]
30. Zhai, Q.; Xie, S.; Fan, W.; Zhang, Q.; Wang, Y.; Deng, W.; Wang, Y. Photocatalytic conversion of carbon dioxide with water into methane: Platinum and copper(I) oxide co-catalysts with a core-shell structure. *Angew. Chem. Int. Ed.* **2013**, *52*, 5776–5779. [[CrossRef](#)]
31. Ali, H.; Guler, A.C.; Masar, M.; Urbanek, P.; Urbanek, M.; Skoda, D.; Suly, P.; Machovsky, M.; Galusek, D.; Kuritka, I. Solid-state synthesis of direct Z-scheme Cu₂O/WO₃ nanocomposites with enhanced visible-light photocatalytic performance. *Catalysts* **2021**, *11*, 293. [[CrossRef](#)]
32. Hao, J.; Qi, B.; Wei, J.; Li, D.; Zeng, F. A Z-scheme Cu₂O/WO₃ heterojunction for production of renewable hydrocarbon fuel from carbon dioxide. *Fuel* **2021**, *287*, 119439. [[CrossRef](#)]
33. Zhang, J.; Ma, H.P.; Liu, Z.F. Highly efficient photocatalyst based on all oxides WO₃/Cu₂O heterojunction for photoelectrochemical water splitting. *Appl. Catal. B* **2017**, *201*, 84–91. [[CrossRef](#)]
34. Guo, J.; Wan, Y.; Zhu, Y.; Zhao, M.; Tang, Z. Advanced photocatalysts based on metal nanoparticle/metalorganic framework composites. *Nano Res.* **2021**, *14*, 2037–2052. [[CrossRef](#)]
35. Cho, H.; Kim, W.D.; Yu, J.; Lee, S.; Lee, D.C. Molecule-driven shape control of metal co-catalysts for selective CO₂ conversion photocatalysis. *ChemCatChem* **2018**, *10*, 5679–5688. [[CrossRef](#)]
36. Qiu, G.; Wang, R.; Han, F.; Tao, X.; Xiao, Y.; Li, B. One-step synthesized Au-Bi₂WO₆ hybrid nanostructures: Synergistic effects of Au nanoparticles and oxygen vacancies for promoting selective oxidation under visible light. *Ind. Eng. Chem. Res.* **2019**, *58*, 17389–17398. [[CrossRef](#)]
37. Li, R.; Luan, Q.; Dong, C.; Dong, W.; Tang, W.; Wang, G.; Lu, Y. Light-facilitated structure reconstruction on self-optimized photocatalyst TiO₂@BiOCl for selectively efficient conversion of CO₂ to CH₄. *Appl. Catal. B* **2021**, *286*, 119832. [[CrossRef](#)]
38. Wang, S.; Teramura, K.; Hisatomi, T.; Domen, K.; Asakura, H.; Hosokawa, S.; Tanaka, T. Highly selective photocatalytic conversion of carbon dioxide by water over Al-SrTiO₃ photocatalyst modified with silver-metal dual cocatalysts. *ACS Sustain. Chem. Eng.* **2021**, *9*, 9327–9335. [[CrossRef](#)]
39. Albo, J.; Qadir, M.I.; Samperi, M.; Fernandes, J.A.; Pedro, I.D.; Dupont, J. Use of an optofluidic microreactor and Cu nanoparticles synthesized in ionic liquid and embedded in TiO₂ for an efficient photoreduction of CO₂ to methanol. *Chem. Eng. J.* **2021**, *404*, 126643. [[CrossRef](#)]
40. Ojha, N.; Bajpai, A.; Kumar, S. Visible light-driven enhanced CO₂ reduction by water over Cu modified S-doped g-C₃N₄. *Catal. Sci. Technol.* **2019**, *9*, 4598–4613. [[CrossRef](#)]

41. Zhang, J.; Zhang, P.; Wang, T.; Gong, J. Monoclinic WO₃ nanomultilayers with preferentially exposed (002) facets for photoelectrochemical water splitting. *Nano Energy* **2015**, *11*, 189–195. [[CrossRef](#)]
42. Liu, J.; Yu, S.; Zhu, W.; Yan, X. Oxygen vacancy-enhanced visible light-driven photocatalytic activity of TiO₂ sphere-W₁₈O₄₉ nanowire bundle heterojunction. *Appl. Catal. A* **2015**, *500*, 30–39. [[CrossRef](#)]
43. Yue, C.; Zhu, X.; Rigutto, M.; Hensen, E. Acid catalytic properties of reduced tungsten and niobium-tungsten oxides. *Appl. Catal. B* **2015**, *163*, 370–381. [[CrossRef](#)]
44. Lee, K.Y.; Hwang, H.; Shin, D.; Choi, W. Enhanced thermopower wave via nanowire bonding and grain boundary fusion in combustion of fuel/CuO-Cu₂O-Cu hybrid composites. *J. Mater. Chem. A* **2015**, *3*, 5457–5466. [[CrossRef](#)]
45. Mao, Y.; He, J.; Sun, X.; Li, W.; Lu, X.; Gan, J.; Liu, Z.; Gong, L.; Chen, J.; Liu, P.; et al. Electrochemical synthesis of hierarchical Cu₂O stars with enhanced photoelectrochemical properties. *Electrochim. Acta* **2012**, *62*, 1–7. [[CrossRef](#)]
46. Moretti, G.; Beck, H.P. On the Auger parameter of Cu(II) compounds. *Surf. Interface Anal.* **2022**, *54*, 803–812. [[CrossRef](#)]
47. Liu, S.; Xia, J.; Yu, J. Amine-functionalized titanate nanosheet-assembled yolk@shell microspheres for efficient cocatalyst-free visible-light photocatalytic CO₂ Reduction. *ACS Appl. Mater. Interfaces* **2015**, *7*, 8166–8175. [[CrossRef](#)]
48. Liu, J.; Liu, Y.; Liu, N.; Han, Y.; Zhang, X.; Huang, H.; Lifshitz, Y.; Lee, S.-T.; Zhong, J.; Kang, Z. Metal-free efficient photocatalyst for stable visible water splitting via a two-electron pathway. *Science* **2015**, *347*, 970–974. [[CrossRef](#)]
49. Pu, Y.C.; Lin, W.H.; Hsu, Y.-C. Modulation of charge carrier dynamics of Na_xH_{2-x}Ti₃O₇-Au-Cu₂O Z-scheme nanoheterostructures through size effect. *Appl. Catal. B* **2015**, *163*, 343–351. [[CrossRef](#)]
50. Cui, D.; Hao, W.; Chen, J. The synergistic effect of heteroatom doping and vacancy on the reduction of CO₂ by photocatalysts. *ChemNanoMat* **2021**, *7*, 894–901. [[CrossRef](#)]
51. Oropeza, F.E.; Dzade, N.Y.; Pons-Marti, A.; Yang, Z.; Zhang, K.H.L.; de Leeuw, N.H.; Hensen, E.J.M.; Hofmann, J.P. Electronic structure and interface energetics of CuBi₂O₄ photoelectrodes. *J. Phys. Chem. C* **2020**, *124*, 22416–22425. [[CrossRef](#)] [[PubMed](#)]